Spark Ablation Coupled with Powder Aerosolization for the One-Step Preparation of Ru/TiO_2 Catalysts for CO_2 Methanation

Plaifa Hongmanorom[a,*], François Devred[a], Damien P. Debecker[a,*]

[a] Institute of Condensed Matter and Nanosciences–Molecular, Solids and Reactivity (IMCN−MOST), Université catholique de Louvain (UCLouvain), Place Louis Pasteur, 1, box L4.01.09, 1348 Louvain-La-Neuve, Belgium.

[*] Corresponding Authors: Plaifa Hongmanorom (plaifa.hongmanorom@uclouvain.be)
Damien P. Debecker (damien.debecker@uclouvain.be)

Abstract

The preparation of powdery heterogeneous catalysts often involves the use of solvents, costly precursors, and thermal treatments in multi-step processes. Herein, we demonstrate the preparation of Ru nanoparticles on TiO_2 via spark ablation coupled with powder aerosolization, offering a clean and simple route with minimal waste generation and reduced pre- and post-synthesis processing. The as-prepared Ru/TiO_2 catalyst is readily active in CO_2 methanation reaction, achieving CH_4 formation rate of 0.21 $mmol g_{Ru}^{-1} s^{-1}$ and TOF of 0.11 s^{-1} at 200 °C, outperforming the corresponding formulation prepared by wetness impregnation followed by calcination. The enhanced performance is attributed to a higher fraction of surface metallic Ru, as spark ablation under inert atmosphere typically yields metallic Ru nanoparticles. Additionally, Ru nanoparticles in the spark-made catalyst are well-distributed over both anatase and rutile TiO_2, driven by Brownian motion and van der Waals adhesion. By contrast, Ru/TiO_2-WI exhibits preferential Ru layer around rutile TiO_2 due to pre-existing RuO_2-rutile TiO_2 epitaxial interactions formed during calcination. This work highlights a sustainable approach for designing highly active low-temperature CO_2 methanation catalysts, with potential versatility for broader catalytic applications.

Keyword: Spark ablation; Ruthenium; Titania; CO_2 methanation

1. Introduction

The atmospheric concentration of carbon dioxide (CO_2) continues to rise, primarily due to human activities, driving global warming and climate instability. To address this, significant efforts have focused on CO_2 capture and utilization (CCU) to close the anthropogenic carbon cycle. One promising approach is CO_2 hydrogenation with renewable hydrogen (H_2) to produce methane (CH_4), so-called CO_2 methanation, offering both emission reduction and energy storage. In Power-to-Gas (PtG) scenario, surplus renewable electricity powers water electrolysis to generate green hydrogen, which reacts with captured CO_2 to form CH_4, a fuel compatible with existing natural gas infrastructure [1-3]. CO_2 methanation is thermodynamically favorable at low temperatures due to its exothermic nature. However, as it involves an eight-electron transfer (reducing carbon from +4 in CO_2 to -4 in CH_4), it faces significant kinetic barriers under mild conditions [4, 5]. Therefore, an active metal catalyst is essential to activate CO_2 and drive the reaction with sufficient rate and selectivity.

Metal catalysts from groups 8 to 10, such as Ru, Rh, Pd, Ni, Co, and Fe, have been widely explored for CO_2 methanation. Among them, Ru supported on metal oxides are commonly regarded as the most active and selective catalysts for this reaction [2, 6-8]. The support also plays a crucial role in the catalytic performance of Ru catalysts for CO_2 methanation, as it not only helps control and stabilize the dispersion of Ru nanoparticles but also provides sites for CO_2 adsorption and activation [7, 9]. Titanium dioxide (TiO_2) is widely used as a support for Ru-based CO_2 methanation catalysts due to its low cost, high stability, and the ability to tune the catalytic performance through morphological and electronic perturbations [10-13].

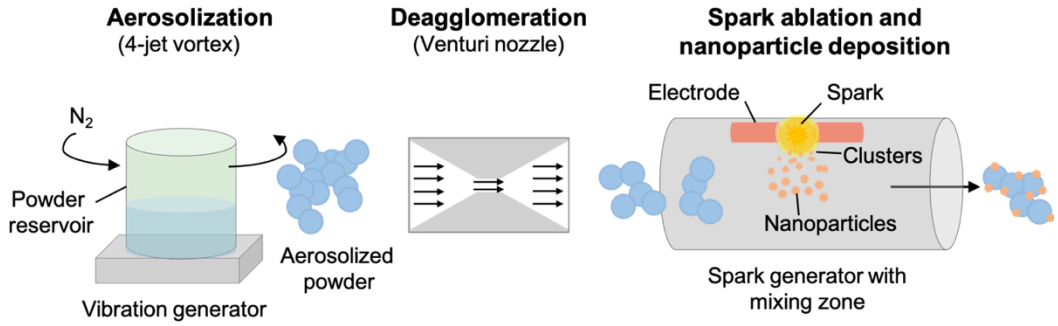
Metal and metal oxide nanoparticles can be synthesized using a variety of approaches. Wet chemical methods, such as chemical reduction, hydrothermal treatment, sol-gel processes, colloidal chemistry, and microwave-assisted techniques, are the most widely used [14-17]. Similarly, supported metal nanoparticles are commonly prepared via wet chemical routes, e.g., impregnation, chemical reduction, deposition-precipitation, and grafting [18-21]. These techniques can offer good control over particle size, shape, and chemical composition but usually require solvents, ligands, or metal precursors, resulting in considerable liquid waste, sometimes containing hazardous by-products. They also involve lengthy batch processes and multiple steps, with thermal treatments and activation (i.e. drying, calcination, reduction) which are particularly energy demanding. As an alternative, physical methods, such as physical vapor deposition, laser ablation, and spark ablation, avoid the use of solvents and chemical precursors altogether. While they can also be energy-intensive, they offer cleaner and more

facile synthesis routes, producing little to no waste and simplifying pre- and post-synthesis steps [22-24].

In recent years, spark ablation has gained attention as an emerging nanotechnology for producing high-purity metals and metal oxides, semiconductor nanoparticles, and nanocomposites, owing to its operational simplicity, scalability, and environmental friendliness [25-27]. The process involves electrical discharges between two electrodes composed of the target material in an inert gas flow, causing rapid vaporization of the electrode material. Controlling the concentration of the evaporated material during the initial stage of particle formation allows tuning the final product from atomic clusters to nanoparticulate agglomerates, enabling good control over nanoparticle sizes [28, 29]. To date, literature has primarily reported the well-controlled deposition of spark-generated nanoparticles on flat surfaces, such as filter media, membranes, and sensor chips [23, 30, 31]. We have recently developed a method for directly depositing metal nanoparticles onto powdery materials by coupling a spark nanoparticle generator with a powder aerosol disperser, enabling the preparation of Ni catalyst deposited on TiO_2 powder [32]. This method is considered a compelling alternative to traditional wetness impregnation because spark ablation provides a solvent-free and precursor-free synthesis route, thereby eliminating drying and calcination steps. Moreover, the rapid nucleation and quenching inherent to spark discharge enable the formation of ultrafine metal nanoparticles (with relatively narrow size distribution) that can be directly deposited onto the support powder. In the present study, we have extended the approach to powdery Ru/TiO_2 catalysts and investigated the catalyst properties and catalytic performance in CO_2 methanation reaction.

2. Results and Discussion

A Ru/TiO_2 catalyst was prepared by depositing spark-ablated Ru nanoparticles onto aerosolized TiO_2 powder (Scheme 1), without further thermal treatment required. It is denoted as "Ru/TiO_2-Spark". For comparison, a Ru/TiO_2 with the same Ru loading as Ru/TiO_2-Spark (0.8wt% measured by ICP-OES, Table 2) was prepared by conventional wetness impregnation, followed by calcination in air at 450 °C to remove residual chlorine (denoted "Ru/TiO_2-WI").



Scheme 1 Schematic representation of the setup coupling spark ablation with powder aerosolization.

2.1. Characterization of Fresh Catalysts

Table 1 Textural properties of TiO_2 support and Ru/TiO_2 catalysts.

Samples	BET surface area (m^2/g)	Total pore volume (cm^3/g)	Average pore diameter (nm)
Pristine TiO_2	50.0	0.20	16
Aerosolized TiO_2	50.5	0.21	16
Ru/TiO_2-WI	48.8	0.49	40
Ru/TiO_2-Spark	50.4	0.19	15

The textural properties of the TiO_2 support and Ru/TiO_2 catalysts were analyzed by N_2 physisorption (Figure 1(a) and (b) and Table 1). All N_2 physisorption isotherms correspond to type IV with an H3 hysteresis loop, attributed to interparticle voids between aggregates of non-porous TiO_2 crystallites [33, 34]. The pristine TiO_2 refers to commercial non-porous P25 TiO_2 powder, which typically has a BET surface area of 50 m^2/g and total pore volume of 0.20 cm^3/g (corresponding to inter-crystallites voids). To determine whether powder aerosolization by the 4-jet vortex 3D tube, followed by deagglomeration in the venturi tube, could influence the textural properties (e.g., if smaller TiO_2 particles were preferentially selected during aerosolization), commercial P25 TiO_2 powder was aerosolized using the powder aerosol disperser without spark ablation. The BET surface area, total pore volume, and average pore diameter of the aerosolized TiO_2 are nearly unchanged after aerosolization and deagglomeration. These properties of Ru/TiO_2-Spark also remain similar after deposition of low-loading Ru onto TiO_2 by spark ablation. Given the low Ru loading and the predominantly surface deposition of Ru nanoparticles, the aggregate structure of non-porous TiO_2 powder is preserved, resulting in negligible changes in the textural properties. In contrast, Ru/TiO_2-WI

shows a slight decrease in BET surface area but significant increases in total pore volume and average pore diameter. The pore volume of small pores (2-10 nm) decreases, accompanied by a considerable increase in the pore volume of larger pores located at ca. 40 nm (Figure 1(b)). The impregnation-drying-calcination process may induce changes in interparticle packing or aggregation.

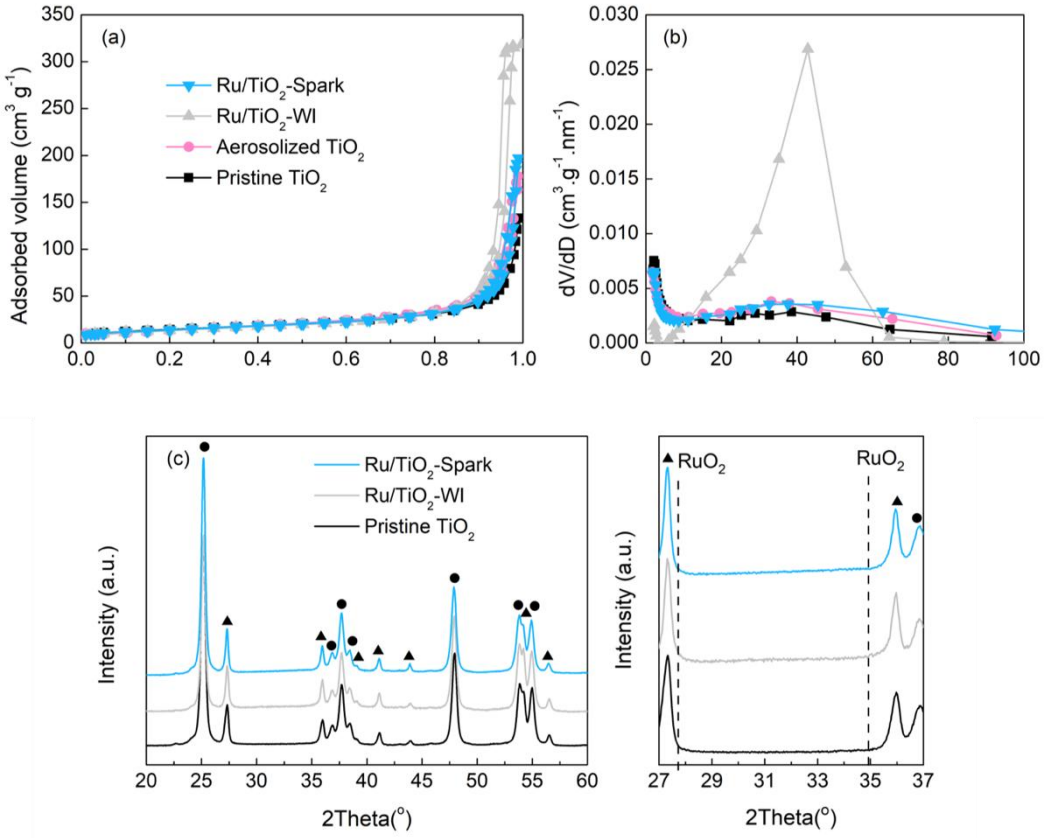


Figure 1 (a) N_2 physisorption isotherms and (b) pore size distribution obtained via the BJH method for pristine TiO_2, aerosolized TiO_2, freshly calcined Ru/TiO_2-WI, and as-prepared Ru/TiO_2-Spark. (c) XRD patterns of pristine TiO_2, freshly calcined Ru/TiO_2-WI, and as-prepared Ru/TiO_2-Spark. Peaks are assigned to anatase TiO_2 (●) and rutile TiO_2 (▲). An enlarged view of the diffraction region from 27-37° is also shown.

The XRD patterns of pristine TiO_2, freshly calcined Ru/TiO_2-WI and as-prepared Ru/TiO_2-Spark catalysts are presented in Figure 1(c). The commercial P25 TiO_2 support exhibits diffraction peaks corresponding to anatase (2θ = 25.4°, 37.0°, 37.8°, 38.6°, 48.1°, 53.9°, and 55.1°) and rutile (2θ = 27.5°, 36.1°, 41.3°, 44.1°, 54.3°, and 56.7°) TiO_2 phases, marketed with 75-85% of anatase and 15-25% of rutile [35]. These diffraction peaks in the XRD patterns of

both Ru/TiO_2 catalysts show no change in intensity, width, or position compared to pristine TiO_2. This indicates that the crystallinity of P25 TiO_2 does not evolve during catalyst preparation (either Spark or WI), consistent with the findings of Kim et al. [12], who reported no change in P25 crystallinity upon annealing $Ru/P25\text{-}TiO_2$ catalyst at 450 °C. Furthermore, no diffraction peaks corresponding to crystalline RuO_2 ($2\theta = 27.7°$ and 34.9°) are observed in the enlarged 27-37° region for either Ru/TiO_2 catalyst, likely due to the low Ru loading. The absence of these peaks also suggests that the RuO_2 crystallites are smaller than 5 nm.

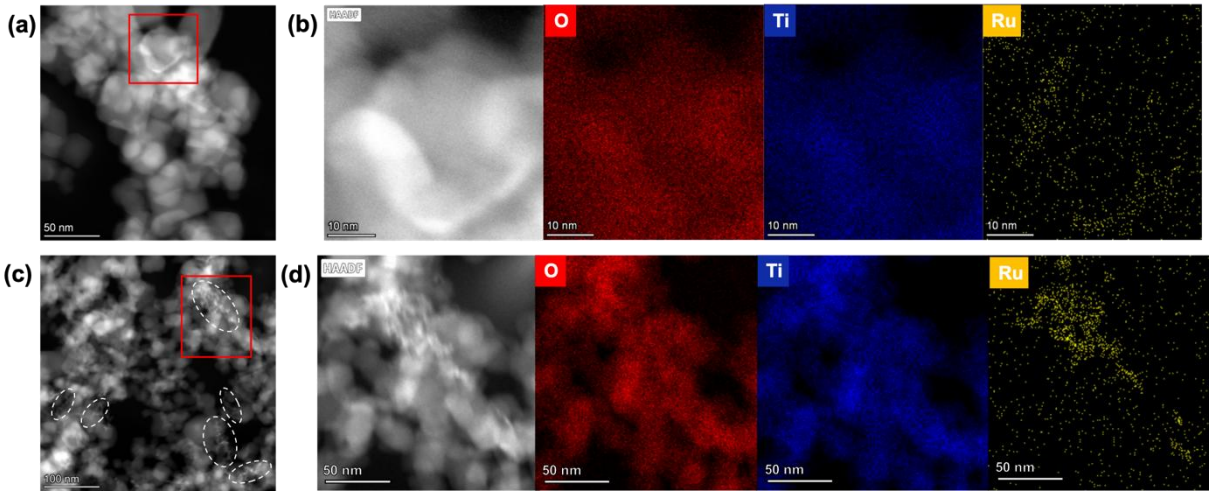


Figure 2 (a) HAADF-STEM image of freshly calcined Ru/TiO_2-WI. (b) HAADF-STEM-EDS elemental (O, Ti, and Ru) mapping data of the selected area (red box) in (a). (c) HAADF-STEM image of as-prepared Ru/TiO_2-Spark. (d) HAADF-STEM-EDS elemental (O, Ti, and Ru) mapping data of the selected area (red box) in (d).

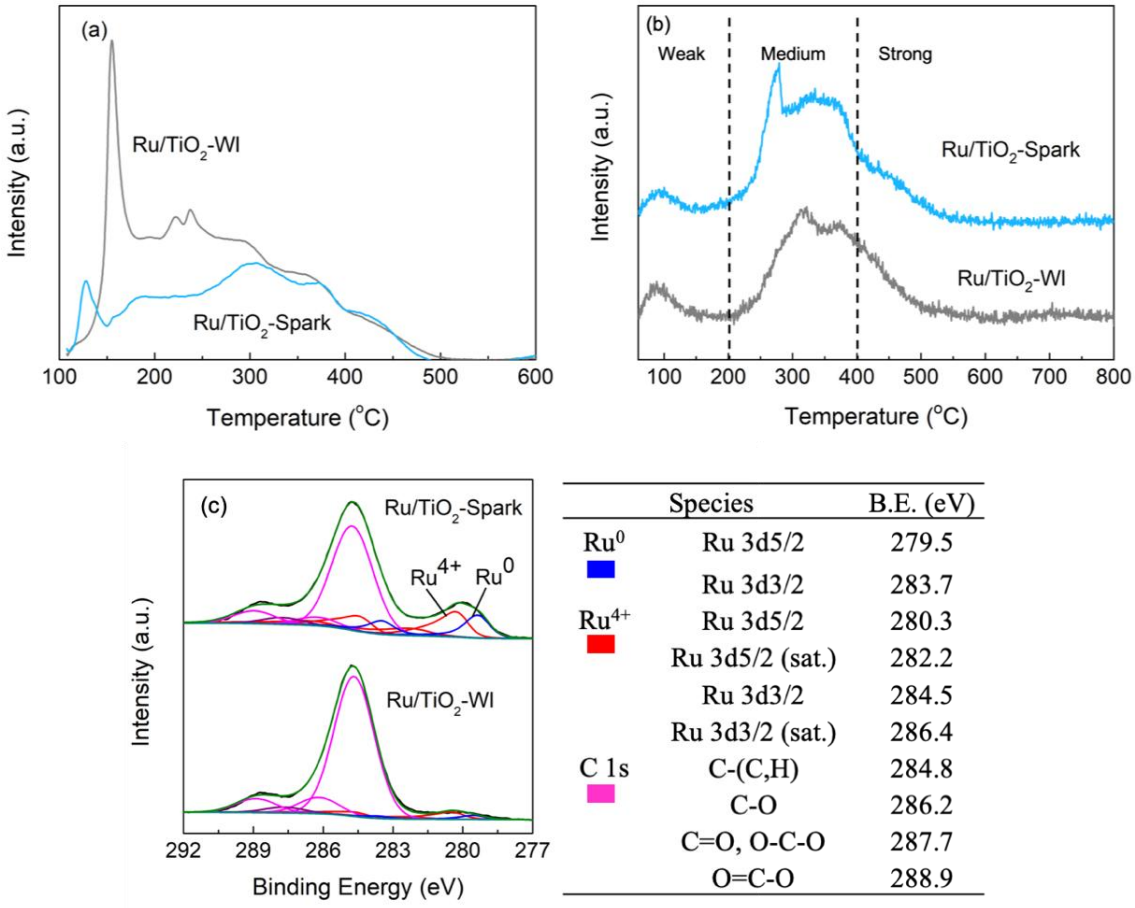
The morphology of freshly calcined Ru/TiO_2-WI and as-prepared Ru/TiO_2-Spark catalysts, as well as the dispersion of Ru species on the TiO_2 surface, are shown in TEM and HAADF-STEM images (Figure 2 and Figure S5). In TEM, it is challenging to distinguish RuO_2 nanoparticles in Ru/TiO_2-WI due to the weak contrast between RuO_2 and TiO_2 (Figure S5(a)). Additionally, HAADF-STEM-EDS images show that only trace amounts of Ru are detected on most TiO_2 particles (Figure S5(c)), while some TiO_2 particles are covered by a thin RuO_2 layer (Figure 2(b)). This observation is in line with previous reports on the redistribution of RuO_2 on P25 TiO_2 upon thermal treatment [12, 36, 37], in which RuO_2 preferentially forms epitaxial layers on the surface of rutile TiO_2 (20% of the P25 support) due to their lattice-matched interfacial structure, whereas anatase TiO_2 phase (80% of the P25 support) remains mostly free of Ru. In contrast, on Ru/TiO_2-Spark, agglomerates of ultrafine (~2 nm) Ru

nanoparticles distributed are clearly visible in TEM and HAADF-STEM images all over the TiO_2 support (highlighted by white dashed ellipses in Figure S5(b) and Figure 2(c)). This is because metal nanoparticles generated via spark ablation of metal electrodes under inert conditions are mainly in the metallic state [28, 38] and deposit indistinctly on TiO_2 anatase and rutile. Since metallic Ru has a higher electron density than RuO_2, the contrast between Ru and TiO_2 is more pronounced than that between RuO_2 and TiO_2. HAADF-STEM-EDS elemental mapping (Figure 2(d)) further confirms the presence of Ru dispersed on the surface of TiO_2 support.

Table 2 Ru loading, Ru dispersion, Ru particle size, CH_4 formation rate, and TOF at 200 °C of Ru/TiO_2 catalysts.

Catalysts	Ru loading (wt%)[a]	Ru dispersion (%)[b]	Ru particle size (nm)[b]	CH_4 formation rate ($mmol g_{Ru}^{-1} s^{-1}$)	TOF (s^{-1})[c]
Ru/TiO_2-WI	0.84	31.6	4.1	0.18	0.06
Ru/TiO_2-Spark	0.79	19.1	6.8	0.21	0.11

[a] Ru loading was determined by ICP-OES. [b] Ru dispersion was obtained from H_2 pulse chemisorption measurement, and the corresponding Ru particle size was calculated as described elsewhere [37, 39]. [c] Turnover frequency (TOF) was calculated from the respective CH_4 formation rate normalized per mole of surface Ru.



	Species	B.E. (eV)
Ru^0	Ru 3d5/2	279.5
	Ru 3d3/2	283.7
Ru^{4+}	Ru 3d5/2	280.3
	Ru 3d5/2 (sat.)	282.2
	Ru 3d3/2	284.5
	Ru 3d3/2 (sat.)	286.4
C 1s	C-(C,H)	284.8
	C-O	286.2
	C=O, O-C-O	287.7
	O=C-O	288.9

Figure 3 (a) H_2-TPR profiles of freshly calcined Ru/TiO_2-WI and as-prepared Ru/TiO_2-Spark catalysts. (b) CO_2-TPD profiles of Ru/TiO_2-WI and Ru/TiO_2-Spark catalysts pre-reduced at 200 °C. (c) XPS spectra of C 1s and Ru 3d regions of freshly calcined Ru/TiO_2-WI and as-prepared Ru/TiO_2-Spark catalysts.

H_2-TPR provides insights into the reducibility of Ru-based catalysts and the interaction between RuO_2 and TiO_2 (Figure 3(a)). The total H_2 consumption (Table 3) of Ru/TiO_2-Spark (0.052 mmol/g_{cat}) is lower than that of Ru/TiO_2-WI (0.083 mmol/g_{cat}). These results could be attributed to Ru species in the spark-prepared catalyst already being in the metallic state, even if partial surface oxidation of metallic Ru inevitably occurs upon exposure to air during sample transfer and storage. Both Ru/TiO_2-WI and Ru/TiO_2-Spark catalysts exhibit complex reduction profiles, likely due to the presence of Ru species with different sizes and different degrees of interaction with TiO_2 support [12, 40]. The peaks between 100-250 °C correspond to the reduction of surface RuO_2 to metallic Ru, while those between 300-500 °C are associated with the reduction of interfacial RuO_x species interacting with TiO_2 support [10, 41]. Within the 100-250 °C, multiple distinct reduction peaks are observed, arising from the distribution of

different RuO_2 particle sizes [40, 41]. When comparing two catalysts, the high-temperature peaks (300-500 °C) are similar, whereas the low-temperature peaks (100-250 °C) are shifted to lower temperatures for Ru/TiO_2-Spark, indicating enhanced reducibility.

Table 3 H_2 consumption from H_2-TPR profiles and proportion of metallic Ru and Ru/Ti ratio measured by XPS before and after CO_2 methanation for Ru/TiO_2 catalysts.

Catalysts	H_2 consumption ($mmol/g_{cat}$)	XPS (Fresh)		XPS (Spent)	
		Ru^0/Ru_{total}	Ru/Ti	Ru^0/Ru_{total}	Ru/Ti
Ru/TiO_2-WI	0.083	0.23	0.02	0.38	0.01
Ru/TiO_2-Spark	0.052	0.34	0.05	0.60	0.03

CO_2-TPD experiments were performed to evaluate the surface basicity of Ru/TiO_2 catalysts. CO_2-TPD profiles (Figure 3(b)) of both Ru/TiO_2-WI and Ru/TiO_2-Spark catalysts display three desorption regions at 50-200 °C, 200-400 °C, and above 400 °C, corresponding to weak, medium, and strong basic sites, respectively [42, 43]. Their relative intensities and desorption temperatures do not differ much, indicating that the surface basicity is not significantly affected by these two different preparation methods.

XPS measurements on freshly calcined Ru/TiO_2-WI and as-prepared Ru/TiO_2-Spark catalysts provide details of their surface composition and the oxidation state of Ru species. Deconvolution of the Ru 3d and C 1s spectra identifies three components: metallic Ru^0, oxidized Ru^{4+}, and the C 1s peak (Figure 3(c)). The Ru 3d envelope contains three doublets: an asymmetric feature at 279.5 eV assigned to metallic Ru^0, and a main doublet at 280.3 eV together with a satellite at 282.2 eV, both associated with Ru^{4+} species [10, 44]. The Ru^0/Ru_{total} and Ru/Ti ratios obtained from XPS are summarized in Table 3. The Ru^0/Ru_{total} ratio is higher for the as-prepared Ru/TiO_2-Spark than for the freshly calcined Ru/TiO_2-WI, indicating a greater fraction of surface metallic Ru and consistent with its lower H_2 consumption in the H_2-TPR profile. In addition, the as-prepared Ru/TiO_2-Spark exhibits higher Ru/Ti ratio than the freshly calcined Ru/TiO_2-WI, in agreement with TEM and HAADF-STEM observations showing that RuO_2 accumulates on rutile TiO_2 in the latter, while Ru nanoparticles are well-distributed across TiO_2 surface in the former.

2.2. Catalytic performance in CO_2 methanation

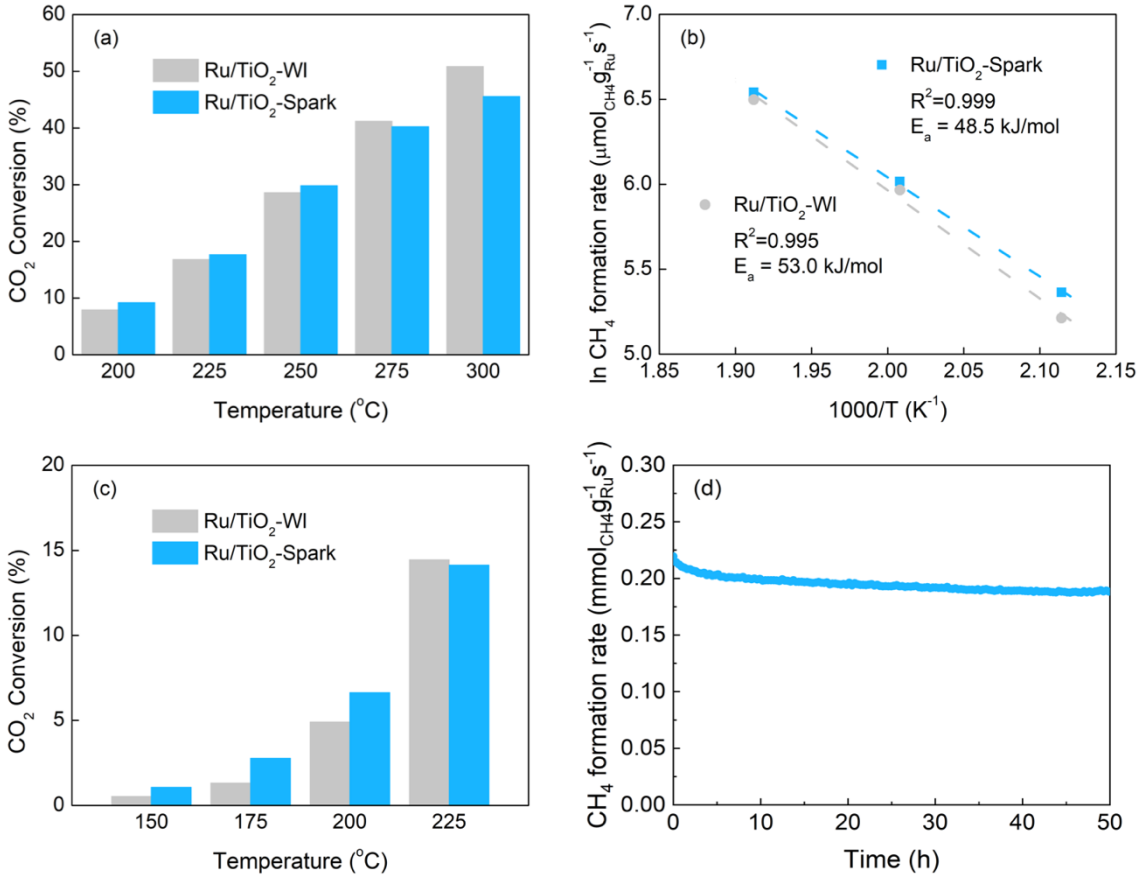


Figure 4 (a) CO_2 conversion at 200-300 °C with pre-reduction at 200 °C. (b) Arrhenius plot of CH_4 formation rate over Ru/TiO_2-WI and Ru/TiO_2-Spark catalysts. (c) CO_2 conversion at 150-225 °C without pre-reduction. (d) CH_4 formation rate at 200 °C for 50 h over Ru/TiO_2-Spark catalyst with pre-reduction at 200 °C.

CO_2 methanation was evaluated between 200 °C and 300 °C to access catalytic activity and selectivity. The reaction conditions were selected to ensure that CO_2 conversion stayed far below the thermodynamic equilibrium limit. Under these conditions, both Ru/TiO_2-WI and Ru/TiO_2-Spark catalysts exhibit complete selectivity toward CH_4 across the entire temperature range. Their CO_2 conversion is comparable between 200 °C and 275 °C, with Ru/TiO_2-WI being slightly more active at 300 °C (Figure 4(a)). The slightly lower CO_2 conversion of Ru/TiO_2-Spark at 300 °C may be attributed to partial growth of Ru nanoparticles under high reaction temperature (vide infra, Section 2.3.). The CH_4 formation rate and turnover frequency (TOF) at 200°C are summarized in Table 2. Ru/TiO_2-Spark achieves CH_4 formation rate of 0.21 $mmol g_{Ru}^{-1} s^{-1}$ and TOF of 0.11 s^{-1}, both higher than those of Ru/TiO_2-WI catalyst (0.18 $mmol g_{Ru}^{-1} s^{-1}$ and 0.06 s^{-1}, respectively). The apparent activation energies (E_a), derived from

the Arrhenius plot (Figure 4(b)), are 53.0 kJ/mol for Ru/TiO_2-WI and 48.5 kJ/mol for Ru/TiO_2-Spark, both within the range typically reported for Ru/TiO_2 catalysts in CO_2 methanation [10-12, 37, 45]. The similar E_a values suggest that the reaction mechanism in Ru/TiO_2-Spark is the same as that in Ru/TiO_2-WI [11, 12]. Table 4 shows that the spark-made Ru/TiO_2 catalyst exhibits a comparable or even superior CH_4 formation rate compared with reported Ru-based CO_2 methanation catalysts. Since Ru nanoparticles formed during spark ablation are already in the metallic state (even if surface passivation occurs afterwards) and the reactant mixture contains H_2, the reaction was also conducted without pre-reduction under H_2, bypassing the activation step often required for conventional methanation catalysts. CO_2 methanation activity can be observed as low as 150 °C (Figure 4(c)), with Ru/TiO_2-Spark showing higher conversion at lower temperatures (150-200 °C). Above 200 °C, CO_2 conversion of both catalysts noticeably increases, reaching comparable levels at 225 °C. The diminished activity gap at elevated temperature may be attributed to an increase in the fraction of surface metallic Ru in the non-pre-reduced Ru/TiO_2-WI catalyst. These results demonstrate that the spark-made Ru/TiO_2 catalyst is readily active and more efficient for low-temperature CO_2 methanation. To evaluate the long-term stability of the spark-made Ru/TiO_2 catalyst, a 50 h time-on-stream test was performed at 200 °C with pre-reduction at 200 °C (Figure 4(d)). The CH_4 formation rate exhibits only a slight decrease from 0.21 to 0.19 $mmolg_{Ru}^{-1}s^{-1}$ over 50 h, indicating that the Ru/TiO_2-Spark catalyst is resistant to sintering or structural changes after extended period under the tested low-temperature reaction conditions.

Table 4 Comparison of CH_4 formation rates with reported Ru-based CO_2 methanation catalysts.

Catalyst	Preparation method	T (°C)	CH_4 formation rate ($mmolg_{Ru}^{-1}s^{-1}$)	Reference
0.8%Ru/TiO_2-WI	Wetness impregnation	200	0.18	This work
0.8%Ru/TiO_2-Spark	Spark ablation	200	0.21	This work
2.4%Ru/TiO_2	Wetness impregnation	200	0.11	[12]
2.2%Ru/TiO_2	Incipient wetness impregnation	210	0.10	[39]
2.2%Ru/TiO_2	Wetness impregnation	200	0.09	[46]
0.4%Ru/ZrO_2-MgO	Wetness impregnation	220	0.26	[47]
2.9%Ru/$Ti_{0.8}Mn_{0.2}O_2$	Wetness impregnation	200	0.25	[48]
2.3%Ru-0.1%Li^+/SiO_2	Co-impregnation	200	0.16	[49]
2.1%Ru/ZrO_2	Incipient wetness impregnation	190	0.14	[50]
2.3%Ru/γ-Al_2O_3	Incipient wetness impregnation	190	0.04	[51]

2.3. Characterization of Spent Catalysts

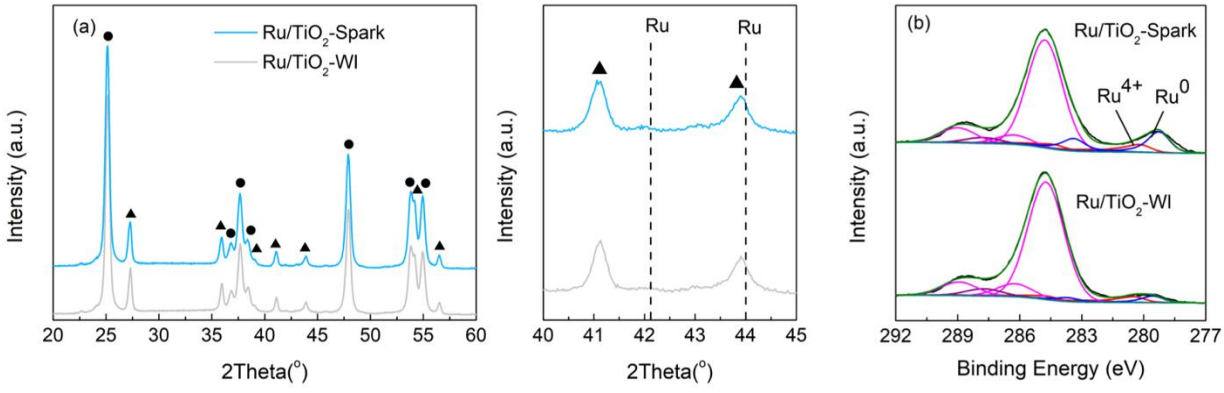


Figure 5 (a) XRD patterns of spent Ru/TiO_2-WI and Ru/TiO_2-Spark catalysts. Peaks are assigned to TiO_2 anatase (●) and TiO_2 rutile (▲). An enlarged view of the diffraction region from 40-45° is also shown. (b) XPS spectra of C 1s and Ru 3d regions of spent Ru/TiO_2-WI and Ru/TiO_2-Spark catalysts after methanation reaction at 150-225 °C without pre-reduction.

After the methanation reaction at 150-225 °C, the spent catalysts were characterized by XRD, XPS, and HAADF-STEM. The XRD diffractograms of the spent catalysts (Fig. 5(a)) show that the crystallinity of anatase and rutile TiO_2 phases remains unchanged. A very small and broad peak at 42.1°, attributed to metallic Ru, is discernible in the enlarged 40-45° region, while the main Ru peak at 44.0° overlaps with the rutile TiO_2 peak, preventing reliable estimation of Ru crystallite size by the Scherrer equation. XPS analysis (Figure 5(b) and Table 3) reveals an increased proportion of surface metallic Ru, indicating reduction of oxidized Ru into Ru^0 during CO_2 hydrogenation. The Ru/Ti ratio slightly decreases for both catalysts, suggesting mild agglomeration of Ru nanoparticles. Nevertheless, as in the fresh catalysts, Ru/TiO_2-Spark retains higher Ru/Ti ratio after the reaction, indicating a greater surface Ru concentration. These findings are consistent with HAADF-STEM observations (Figure 6). In the spent Ru/TiO_2-WI, smaller Ru nanoparticles (~ 2-4 nm) preferentially concentrate around rutile TiO_2 particles due to pre-existing RuO_2-rutile TiO_2 epitaxial interactions (Figure 6(a)). By contrast, larger Ru nanoparticles (~ 2-10 nm) in the spent Ru/TiO_2-Spark are well-distributed over both anatase and rutile TiO_2 particles (Figure 6(b) and Figure S6). Ru dispersion and Ru particle sizes were also determined by H_2 pulse chemisorption (Table 2). The estimated Ru particle sizes in Ru/TiO_2-WI (4.1 nm) and Ru/TiO_2-Spark (6.8 nm) catalysts are in line with those observed from HAADF-STEM images. It is noted that when the Ru/TiO_2-Spark catalyst underwent methanation reaction at 200-300 °C with pre-reduction at 200 °C, Ru nanoparticles larger than 10 nm are observable in HAADF-STEM image (Figure S7), indicating Ru particle growth under high reaction temperature.

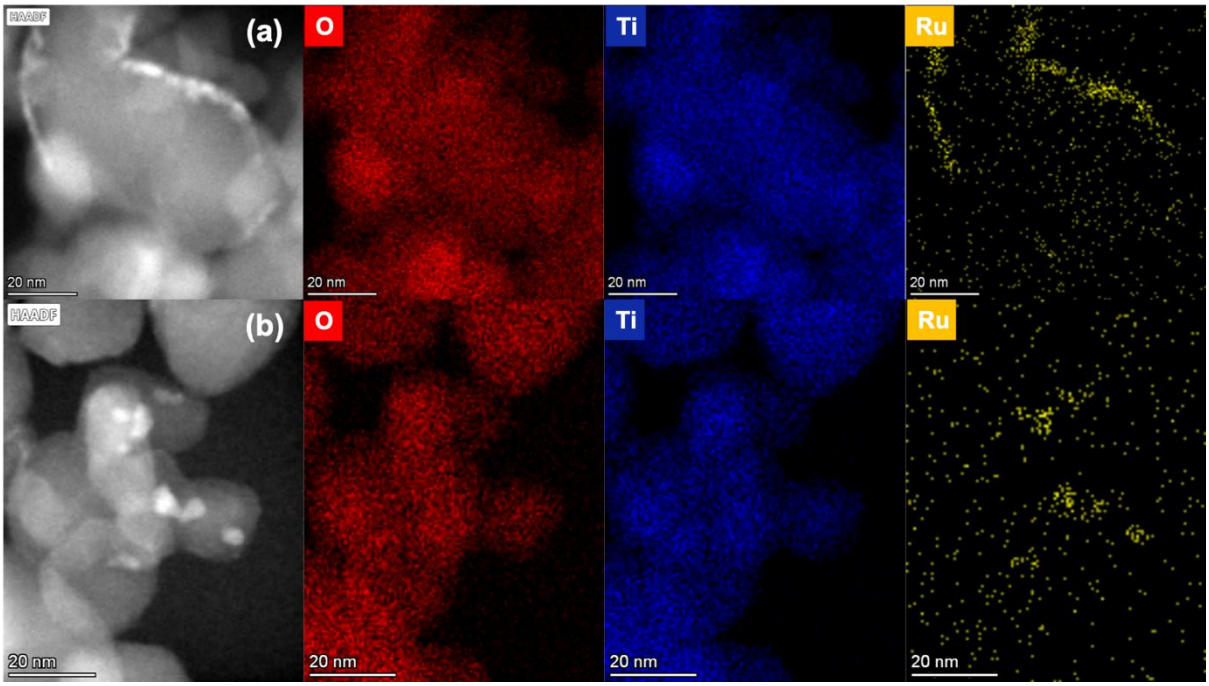


Figure 6 HAADF-STEM-EDS elemental (O, Ti, and Ru) mapping data of the spent (a) Ru/TiO_2-WI and (b) Ru/TiO_2-Spark catalysts after methanation reaction at 150-225 °C without pre-reduction.

2.4. Decisive factors dictating the methanation activity

The Ru/TiO_2 catalysts prepared by wetness impregnation and by spark ablation coupled with powder aerosolization both exhibit the same 100% selectivity toward CH_4 but distinctive level of low-temperature CO_2 methanation activity. At 200 °C, Ru/TiO_2-Spark shows higher CH_4 formation rate despite its lower Ru dispersion. When normalized to the number of exposed Ru sites, its turnover frequency (TOF) is also higher, indicating that spark-ablated Ru nanoparticles deposited on TiO_2 provide greater intrinsic activity per active site than Ru nanoparticles supported on TiO_2 prepared by wetness impregnation.

Methanation is considered a structure-sensitive reaction. XPS and HAADF-STEM analyses reveal distinct structural modifications between Ru/TiO_2-WI and Ru/TiO_2-Spark during catalyst preparation and under methanation conditions (Figure 7). For the catalyst prepared by wetness impregnation, calcination in air at 450 °C is necessary to remove residual chlorine. This step induces the formation and redistribution of RuO_2 nanoparticles, which preferentially grow as epitaxial layers around rutile TiO_2 due to their lattice matching, leaving anatase TiO_2 largely RuO_2-free. Upon CO_2 hydrogenation, these RuO_2 epitaxial layers are reduced, but Ru remains localized as small nanoparticles over rutile TiO_2 particles. For the catalyst prepared by spark ablation, Ru nanoparticles are generated via spark discharges between Ru electrodes. The

resulting Ru vapor cloud is rapidly quenched by an inert gas flow and condensed into clusters and small nanoparticles through particle-particle collisions and coalescence. The Ru nanoparticles stream then encounters the aerosolized TiO_2 powder stream in the mixing zone, where Ru nanoparticles undergo Brownian motion, collide with TiO_2, and adhere via van der Waals interactions [38, 52]. This process enables Ru nanoparticles to deposit on both anatase and rutile TiO_2. Although some agglomeration occurs during CO_2 hydrogenation, Ru nanoparticles remain well-distributed across TiO_2 support. Notably, no epitaxial layer growth of Ru over rutile TiO_2 is observed in Ru/TiO_2-Spark, likely due to the lack of lattice matching between metallic Ru and rutile TiO_2. This observation aligns with literature reports that RuO_2-rutile TiO_2 epitaxial interactions arise specifically during calcination. Indeed, direct reduction of Ru/TiO_2 without prior calcination suppresses such epitaxial lattice matching [10]. Considering these structural modifications, higher TOF of Ru/TiO_2-Spark suggests that Ru nanoparticles produced by spark ablation possess more intrinsically active surface Ru sites. This likely arises from the distribution of Ru nanoparticles across both anatase and rutile TiO_2, which may create more favorable metal-support interface, compared to Ru/TiO_2-WI where Ru nanoparticles are predominantly located on rutile phase.

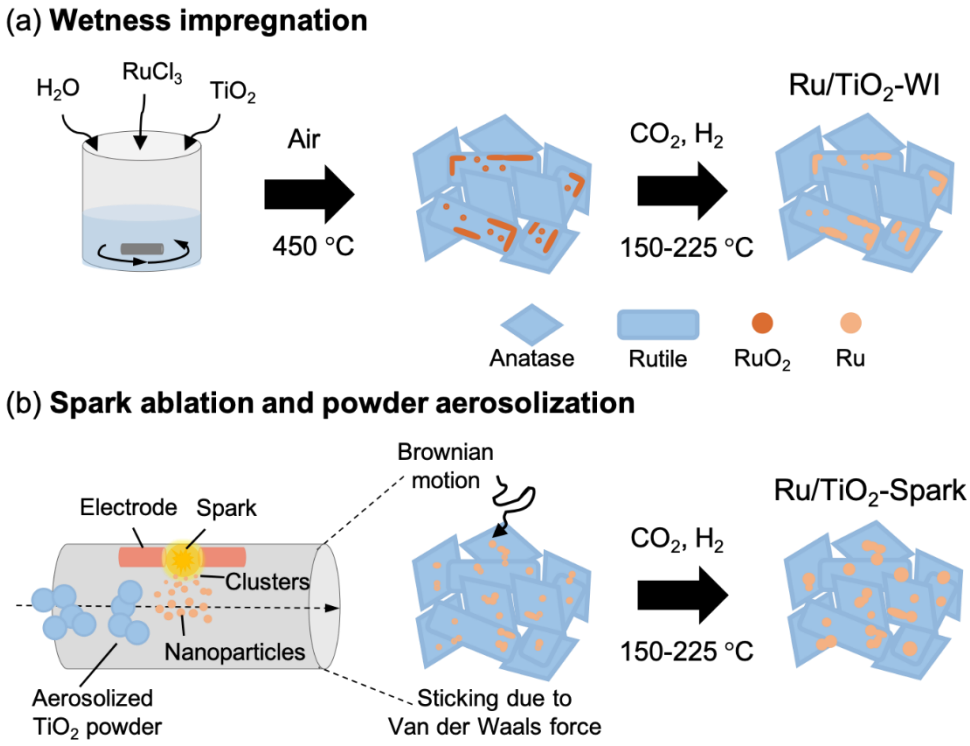


Figure 7 Graphical illustration of the evolution of Ru species in (a) Ru/TiO_2-WI catalyst after wetness impregnation, calcination, and CO_2 methanation reaction and (b) Ru/TiO_2-Spark

catalyst after spark ablation coupled with powder aerosolization, metal nanoparticle deposition via Brownian motion and van der Waals force, and CO_2 methanation reaction.

In several studies, methanation activity has been shown to increase with Ru particle size. For instance, Szanyi et al. investigated a series of Ru/Al_2O_3 catalysts with different subnanometer-sized metal atoms and clusters, controlled by varying Ru content between 0.1 and 5 wt%. They found that larger Ru clusters on $5\%Ru/Al_2O_3$ were more active and selective than smaller Ru clusters on $0.5\%Ru/Al_2O_3$ [53]. Similarly, Panagiotopoulou et al. reported that TOF of CO_2 during CO/CO_2 co-methanation was significantly improved with increasing Ru crystallite size on Ru/TiO_2 from 2.1 nm (0.5 wt% Ru) to 4.5 nm (5 wt% Ru) [54]. The superior methanation performance has been attributed to less formation of unreactive CO_{ad} on low-coordinated Ru sites and higher concentration of reactive linear carbonyl species [55, 56]. Further exploration of this aspect will be necessary in future studies.

3. Conclusions

Ru nanoparticles supported on TiO_2 were prepared using the spark-ablation nanoparticle generator coupled with the powder aerosol disperser. This precursor-free and solvent-free approach minimizes waste generation. Moreover, energy-demanding calcination and reduction steps are unnecessary, as metallic Ru nanoparticles are readily produced via spark ablation under an inert atmosphere. The as-prepared Ru/TiO_2-Spark catalyst is readily active in low-temperature CO_2 methanation. It achieves higher CH_4 formation rate and TOF compared to the catalyst prepared by conventional wetness impregnation, which could be dictated by chemical and structural properties. This study provides an insight into distinct structural modifications between these two catalysts during catalyst preparation and under methanation conditions. In Ru/TiO_2-Spark, Ru nanoparticles are well-distributed across both anatase and rutile TiO_2. In contrast, Ru/TiO_2-WI shows preferential deposition of Ru on rutile TiO_2, arising from RuO_2-rutile TiO_2 epitaxial interactions established during calcination. Overall, spark ablation coupled with powder aerosolization offers a sustainable synthesis strategy, with potential to be extended to other metals and metal oxide supports for a wide range of catalytic applications.

4. Experimental Section

4.1. Preparation of Catalysts

Titanium dioxide, P25 TiO_2 (Degussa), was used as a support material after being freshly calcined in air at 500 °C (5 °C/min) for 5 h. Ru electrodes (3mm diameter; 99.99% purity) were used as a source for generating Ru nanoparticles. The preparation of spark-ablated Ru/TiO_2 catalyst is illustrated in Scheme 1, with detailed descriptions provided in the Supporting Information (Figure S1-S4). The TiO_2 powder in the reservoir is first dispensed and aerosolized using a 4-jet vortex with N_2 and then gas-transported through a Venturi nozzle for deagglomeration before being injected into the spark ablation generator. Within the generator, spark discharges between Ru electrodes produce Ru clusters that aggregate into nanoparticles, which are subsequently deposited onto injected TiO_2 particles in the mixing zone. The resulting Ru/TiO_2-Spark catalyst is finally collected on a membrane filter (Durapore®, PVDF with 0.45 μm pore size).

For comparison, Ru/TiO_2 was prepared by a conventional wetness impregnation. First, 0.042 g of $RuCl_3 \cdot H_2O$ was dissolved in 10 mL of distilled water. After stirring until complete dissolution, 1 g of commercial P25 TiO_2 was added into the solution and stirred for 16 h at 50 °C. The solution was then dried in a rotavapor at 50 °C before calcination in air at 450 °C (5 °C/min) for 5 h, yielding Ru/TiO_2-WI catalyst.

4.2. Characterization of Catalysts

Nitrogen physisorption measurements were performed at -196 °C using a Micromeritics Tristar 3000 analyzer to access the textural properties. Prior to analysis, 100 mg of sample was degassed under vacuum at 200 °C overnight to remove physisorbed water and volatile compounds. The specific surface area was calculated using the Brunauer–Emmett–Teller (BET) method within a relative pressure (P/P_0) range of 0.05–0.3. Total pore volume was determined from the adsorption data at $P/P_0 \approx 0.98$, while the average pore diameter was derived using the Barrett–Joyner–Halenda (BJH) method from the adsorption branch of the isotherm.

X-ray diffraction (XRD) analysis was conducted using a Bruker AXS-D8 Advance diffractometer equipped with Cu Kα radiation ($\gamma = 1.78$ Å), operated at 35 kV and 40 mA. Data were collected over a 2θ range of 20-60°, with a step size of 0.025° and a step time of 20 seconds per step.

Transmission electron microscopy (TEM) and high-angle annular dark-field scanning transmission electron microscopy (HAADF-STEM), along with energy-dispersive X-ray spectroscopy (EDX) analysis, were conducted at 200 kV using a Talos F200i transmission electron microscope. VELOX software was used for data acquisition and analysis.

The ruthenium content in the catalyst was quantified by inductively coupled plasma optical emission spectroscopy (ICP-OES) using a Perkin Elmer Avio220 max instrument. Prior to analysis, the samples were digested with bleach for 30 min, treated with HCl, and subsequently solubilized in HBF_4 and HNO_3 to ensure complete dissolution of Ru and TiO_2.

H_2-temperature programmed reduction (H_2-TPR) was performed on a BELCAT II instrument (Microtrac). Around 50 mg of the catalyst was first pre-treated in a 50 mL/min argon stream at 200 °C to eliminate adsorbed moisture and surface contaminants. After cooling to 100 °C, the reduction profile was recorded while heating the sample from 100 °C to 600 °C at a rate of 10 °C/min in a flow of 1% H_2 in Ar (50 mL/min).

CO_2-temperature programmed desorption (CO_2-TPD) was performed on a BELCAT II instrument (Microtrac). Around 80 mg of the catalyst was first purged under Ar (30 mL/min), followed by reduction at 200 °C in 5%H_2/Ar (30 mL/min) for 1 h. The sample was then purged under Ar (30 mL/min) to remove residual H_2 and cooled to 50 °C. Subsequently, it was exposed to 16.7% CO_2/Ar gas stream for 1 h, after which physically adsorbed CO_2 was removed by purging under Ar (30 mL/min). The desorption profile was recorded by monitoring the MS signal (m/z = 44) while heating the sample to 800 °C at a rate of 10 °C/min.

H_2 pulse chemisorption measurement was carried out using a BELCAT II system (Microtrac). Approximately 70 mg of catalyst was packed into a quartz reactor and pre-treated at 200 °C for 2 hours under a 30 mL/min flow of 5% H_2 in Ar. This was followed by an argon purge at the same temperature and flow rate for 1 h. After cooling the sample to 100 °C, H_2 was introduced in pulses using a 0.989 mL loop until saturation was reached. Ru dispersion was determined assuming a H/Ru stoichiometric ratio of 1.

X-ray photoelectron spectroscopy (XPS) was performed on a Surface Science Instruments SSX 100/206 system using Al-Kα radiation (10 kV, 20 mA). The C 1s peak at 284.8 eV was used for binding energy calibration. Data treatment and peak fitting were carried out using CasaXPS software.

4.3. Catalytic Tests

Catalytic performance was assessed using a continuous-flow fixed-bed reactor (a 6 mm internal diameter Stainless steel tube). Initially, 80 mg of catalyst was pre-reduced at 200 °C under H_2 flow (20 mL/min) for 1 h. Subsequently, a reactant gas mixture consisting of 10% CO_2 and 40% H_2 in Ar (total flow rate of 20 mL/min) was introduced. Reaction was carried out at atmospheric pressure across a temperature range of 200 °C to 300 °C in 25 °C increments. The catalytic test was also performed from 150 °C to 225 °C without pre-reduction At each temperature step, steady-state conditions were confirmed by conducting a minimum of four gas chromatograph (GC) analyses. Product gases were analyzed with a SCION 456 GC equipped with Hayesep Q, Molsieve 5A, Porapak R, and SCION-1 columns, using a TCD for CO and CO_2 and an FID for CH_4 detection and quantification. All gas transfer lines were kept at 125 °C to avoid condensation of water vapor. The CO_2 conversion (X_{CO_2}), CH_4 selectivity (S_{CH_4}), CH_4 formation rate (r_{CH_4}), and turnover frequency (TOF) were calculated according to the following equations:

$$X_{CO_2}(\%) = \frac{F_{CO_{2,in}} - F_{CO_{2,out}}}{F_{CO_{2,in}}} \times 100\% \quad (1)$$

$$S_{CH_4}(\%) = \frac{F_{CH_{4,out}}}{F_{CO_{2,in}} - F_{CO_{2,out}}} \times 100\% \quad (2)$$

$$r_{CH_4}\ (mmol_{CO_2} g_{Ru}^{-1} s^{-1}) = \frac{F_{CH_{4,out}}}{m_{Ru}} \quad (3)$$

$$TOF\ (s^{-1}) = \frac{r_{CH_4} \times M_{Ru}}{D_{Ru}} \quad (4)$$

where F is the molar flow rate, m_{Ru} is the mass of Ru measured by ICP-OES, M_{Ru} is the molar mass of Ru (101.07 g/mol), and D_{Ru} is the Ru dispersion determined by H_2 pulse chemisorption.

Acknowledgements

The authors thank Tobias Pfeiffer, Tobias Coppejans, and Sofia Dimitriadou from VSParticle for their assistance in setting up the VSP-G1 spark nanoparticle generator coupled with the powder aerosol disperser, as well as for providing technical support. We also thank Fabio Lucaccioni for his assistance with ICP-OES analysis. Plaifa Hongmanorom acknowledges the Fonds De La Recherche Scientifique – FNRS (10.13039/501100002661) for her postdoctoral researcher – CR fellowship. This work was also supported by the FNRS under Grant GEQ (Large Equipment) – UG01622F. DPD thanks the Francqui Foundation for the Francqui Research Professor chair.

Conflict of Interests

The authors declare no conflict of interest.

References

[1] M. Thema, F. Bauer, M. Sterner, Power-to-Gas: Electrolysis and methanation status review, Renew. Sustain. Energy Rev., 112 (2019) 775-787.
[2] M. Tommasi, S.N. Degerli, G. Ramis, I. Rossetti, Advancements in CO2 methanation: A comprehensive review of catalysis, reactor design and process optimization, Chem. Eng. Res. Des., 201 (2024) 457-482.
[3] K. Ghaib, F.-Z. Ben-Fares, Power-to-Methane: A state-of-the-art review, Renew. Sustain. Energy Rev., 81 (2018) 433-446.
[4] S. Roy, A. Cherevotan, S.C. Peter, Thermochemical CO2 Hydrogenation to Single Carbon Products: Scientific and Technological Challenges, ACS Energy Letters, 3 (2018) 1938-1966.
[5] L. Shen, J. Xu, M. Zhu, Y.-F. Han, Essential Role of the Support for Nickel-Based CO2 Methanation Catalysts, ACS Catal., 10 (2020) 14581-14591.
[6] J. Ashok, S. Pati, P. Hongmanorom, Z. Tianxi, C. Junmei, S. Kawi, A review of recent catalyst advances in CO2 methanation processes, Catal. Today, (2020).
[7] C. Shen, M. Liu, S. He, H. Zhao, C.-j. Liu, Advances in the studies of the supported ruthenium catalysts for CO2 methanation, Chinese Journal of Catalysis, 63 (2024) 1-15.
[8] P. Frontera, A. Macario, M. Ferraro, P. Antonucci, Supported Catalysts for CO2 Methanation: A Review, Catalysts, 7 (2017) 59.
[9] M.P. Almeida, L.V. Mattos, S. Walker, M. Ayala, C.D. Watson, G. Jacobs, R.C. Rabelo-Neto, M. Akri, S. Paul, F.B. Noronha, Unveiling the effect of support on the mechanism of CO2 hydrogenation over supported Ru catalysts, Applied Catalysis B: Environment and Energy, 365 (2025) 124986.
[10] J. Zhou, Z. Gao, G. Xiang, T. Zhai, Z. Liu, W. Zhao, X. Liang, L. Wang, Interfacial compatibility critically controls Ru/TiO2 metal-support interaction modes in CO2 hydrogenation, Nature Communications, 13 (2022) 327.
[11] A. Kim, D.P. Debecker, F. Devred, V. Dubois, C. Sanchez, C. Sassoye, CO2 methanation on Ru/TiO2 catalysts: On the effect of mixing anatase and rutile TiO2 supports, Appl. Catal., B, 220 (2018) 615-625.
[12] A. Kim, C. Sanchez, G. Patriarche, O. Ersen, S. Moldovan, A. Wisnet, C. Sassoye, D.P. Debecker, Selective CO2 methanation on Ru/TiO2 catalysts: unravelling the decisive role of the TiO2 support crystal structure, Catal. Sci. Technol., 6 (2016) 8117-8128.
[13] T.W. van Deelen, C. Hernández Mejía, K.P. de Jong, Control of metal-support interactions in heterogeneous catalysts to enhance activity and selectivity, Nat. Catal., 2 (2019) 955-970.
[14] A.V. Nikam, B.L.V. Prasad, A.A. Kulkarni, Wet chemical synthesis of metal oxide nanoparticles: a review, CrystEngComm, 20 (2018) 5091-5107.
[15] P.G. Jamkhande, N.W. Ghule, A.H. Bamer, M.G. Kalaskar, Metal nanoparticles synthesis: An overview on methods of preparation, advantages and disadvantages, and applications, J. Drug Deliv. Sci. Technol., 53 (2019) 101174.
[16] G. Habibullah, J. Viktorova, T. Ruml, Current Strategies for Noble Metal Nanoparticle Synthesis, Nanoscale Research Letters, 16 (2021) 47.

[17] D.P. Debecker, S. Le Bras, C. Boissière, A. Chaumonnot, C. Sanchez, Aerosol processing: a wind of innovation in the field of advanced heterogeneous catalysts, Chem. Soc. Rev., 47 (2018) 4112-4155.
[18] C. Sassoye, G. Muller, D.P. Debecker, A. Karelovic, S. Cassaignon, C. Pizarro, P. Ruiz, C. Sanchez, A sustainable aqueous route to highly stable suspensions of monodispersed nano ruthenia, Green Chem., 13 (2011) 3230-3237.
[19] M. Balaraju, V. Rekha, B.L.A.P. Devi, R.B.N. Prasad, P.S.S. Prasad, N. Lingaiah, Surface and structural properties of titania-supported Ru catalysts for hydrogenolysis of glycerol, Appl. Catal., A, 384 (2010) 107-114.
[20] P. Zhang, X. Sui, Y. Wang, Z. Wang, J. Zhao, N. Wen, H. Chen, H. Huang, Z. Zhang, R. Yuan, Z. Ding, W. Dai, X. Fu, Y.-X. Weng, J. Long, Surface Ru–H Bipyridine Complexes-Grafted TiO2 Nanohybrids for Efficient Photocatalytic CO2 Methanation, Journal of the American Chemical Society, 145 (2023) 5769-5777.
[21] D. Zhao, S. Lyu, Q. Cheng, Y. Liu, P. Zhao, Q. Zhang, Y. Zhang, Y. Pan, X. Li, S. Xiong, Z. Wang, X. Li, Highly Efficient Assembly-Line Production of Long-Chain Hydrocarbons via Fischer–Tropsch Synthesis over Ru/TiO2 Catalysts, Journal of the American Chemical Society, 147 (2025) 20493-20503.
[22] P.A. Pandey, G.R. Bell, J.P. Rourke, A.M. Sanchez, M.D. Elkin, B.J. Hickey, N.R. Wilson, Physical Vapor Deposition of Metal Nanoparticles on Chemically Modified Graphene: Observations on Metal–Graphene Interactions, Small, 7 (2011) 3202-3210.
[23] S. Drdova, M. Gao, O. Sambalova, R. Pauer, Z. Zhou, S. Dimitriadou, A. Schmidt-Ott, J. Wang, Precursor- and waste-free synthesis of spark-ablated nanoparticles with enhanced photocatalytic activity and stability towards airborne organic pollutant degradation, Environmental Science: Nano, 11 (2024) 1023-1043.
[24] L. Song, Y. Wang, J. Ma, Q. Zhang, Z. Shen, Core/shell structured Zn/ZnO nanoparticles synthesized by gaseous laser ablation with enhanced photocatalysis efficiency, Appl. Surf. Sci., 442 (2018) 101-105.
[25] J. Feng, R. Geutjens, N.V. Thang, J. Li, X. Guo, A. Kéri, S. Basak, G. Galbács, G. Biskos, H. Nirschl, H.W. Zandbergen, E. Brück, A. Schmidt-Ott, Magnetic Phase Transition in Spark-Produced Ternary LaFeSi Nanoalloys, ACS Applied Materials & Interfaces, 10 (2018) 6073-6078.
[26] N.S. Tabrizi, Q. Xu, N.M. van der Pers, U. Lafont, A. Schmidt-Ott, Synthesis of mixed metallic nanoparticles by spark discharge, J. Nanopart. Res., 11 (2009) 1209-1218.
[27] S. Kala, P. Rawat, F.E. Kruis, Viability of spark-discharge technique to produce semiconductor nanoparticles, Materials Today: Proceedings, 28 (2020) 96-99.
[28] T.V. Pfeiffer, J. Feng, A. Schmidt-Ott, New developments in spark production of nanoparticles, Adv. Powder Technol., 25 (2014) 56-70.
[29] C. Loizidis, K.C. Petallidou, A. Maisser, S. Bezantakos, T.V. Pfeiffer, A. Schmidt-Ott, G. Biskos, Insights into the enhancement of nanoparticle production throughput by atmospheric-pressure spark ablation, Aerosol Sci. Technol., 58 (2024) 1421-1431.
[30] F.M. Sapountzi, M. Lavorenti, W. Vrijburg, S. Dimitriadou, B. Tyburska-Pueschel, P. Thüne, H. Niemantsverdriet, T.V. Pfeiffer, M.N. Tsampas, Spark Ablation for the Fabrication of PEM Water Electrolysis Catalyst-Coated Membranes, Catalysts, 12 (2022) 1343.
[31] N.A. Isaac, M. Valenti, A. Schmidt-Ott, G. Biskos, Characterization of Tungsten Oxide Thin Films Produced by Spark Ablation for NO2 Gas Sensing, ACS Applied Materials & Interfaces, 8 (2016) 3933-3939.

[32] D.P. Debecker, P. Hongmanorom, T.V. Pfeiffer, B. Zijlstra, Y. Zhao, S. Casale, C. Sassoye, Spark ablation: a dry, physical, and continuous method to prepare powdery metal nanoparticle-based catalysts, Chem. Commun., 60 (2024) 11076-11079.
[33] G. Zhou, R. Dou, H. Bi, S. Xie, Y. Pei, K. Fan, M. Qiao, B. Sun, B. Zong, Ru nanoparticles on rutile/anatase junction of P25 TiO2: Controlled deposition and synergy in partial hydrogenation of benzene to cyclohexene, J. Catal., 332 (2015) 119-126.
[34] J. Yu, H. Yu, B. Cheng, M. Zhou, X. Zhao, Enhanced photocatalytic activity of TiO2 powder (P25) by hydrothermal treatment, J. Mol. Catal. A: Chem., 253 (2006) 112-118.
[35] M. Umair, A. Ruiz-Aguirre, I. Berruti, S.M. Rodríguez, L. Palmisano, V. Loddo, M. Bellardita, Biomass derivatives photoreforming in pilot plant scale to obtain H2 under green conditions by using ball milling Cu2O-TiO2 P25 photocatalysts, Chem. Eng. J., 504 (2025) 158585.
[36] G. Xiang, X. Shi, Y. Wu, J. Zhuang, X. Wang, Size effects in Atomic-Level Epitaxial Redistribution Process of RuO2 over TiO2, Sci. Rep., 2 (2012) 801.
[37] Z. Zhao, Q. Jiang, Q. Wang, M. Wang, J. Zuo, H. Chen, Q. Kuang, Z. Xie, Effect of Rutile Content on the Catalytic Performance of Ru/TiO2 Catalyst for Low-Temperature CO2 Methanation, ACS Sustainable Chem. Eng., 9 (2021) 14288-14296.
[38] J. Feng, G. Biskos, A. Schmidt-Ott, Toward industrial scale synthesis of ultrapure singlet nanoparticles with controllable sizes in a continuous gas-phase process, Sci. Rep., 5 (2015) 15788.
[39] S. Cisneros, S. Chen, C. Fauth, A.M. Abdel-Mageed, S. Pollastri, J. Bansmann, L. Olivi, G. Aquilanti, H. Atia, J. Rabeah, M. Parlinska-Wojtan, A. Brückner, R.J. Behm, Controlling the selectivity of high-surface-area Ru/TiO2 catalysts in CO2 reduction - modifying the reaction properties by Si doping of the support, Appl. Catal., B, 317 (2022) 121748.
[40] M.A.G. Hevia, A.P. Amrute, T. Schmidt, J. Pérez-Ramírez, Transient mechanistic study of the gas-phase HCl oxidation to Cl2 on bulk and supported RuO2 catalysts, J. Catal., 276 (2010) 141-151.
[41] W. Tolek, N. Nanthasanti, B. Pongthawornsakun, P. Praserthdam, J. Panpranot, Effects of TiO2 structure and Co addition as a second metal on Ru-based catalysts supported on TiO2 for selective hydrogenation of furfural to FA, Sci. Rep., 11 (2021) 9786.
[42] M. Liu, R. Zou, C.-j. Liu, Improvement in the activity of Ru/ZrO2 for CO2 methanation by the enhanced hydrophilicity of zirconia, Applied Catalysis B: Environment and Energy, 360 (2025) 124549.
[43] Q. Li, H. Wang, M. Zhang, G. Li, J. Chen, H. Jia, Suppressive Strong Metal-Support Interactions on Ruthenium/TiO2 Promote Light-Driven Photothermal CO2 Reduction with Methane, Angew. Chem. Int. Ed., 62 (2023) e202300129.
[44] S. Carenco, C. Sassoye, M. Faustini, P. Eloy, D.P. Debecker, H. Bluhm, M. Salmeron, The Active State of Supported Ruthenium Oxide Nanoparticles during Carbon Dioxide Methanation, J. Phys. Chem. C, 120 (2016) 15354-15361.
[45] T. Abe, M. Tanizawa, K. Watanabe, A. Taguchi, CO2 methanation property of Ru nanoparticle-loaded TiO2 prepared by a polygonal barrel-sputtering method, Energy Environ. Sci., 2 (2009) 315-321.
[46] A. Kim, C. Sanchez, B. Haye, C. Boissière, C. Sassoye, D.P. Debecker, Mesoporous TiO2 Support Materials for Ru-Based CO2 Methanation Catalysts, ACS Applied Nano Materials, 2 (2019) 3220-3230.
[47] S. Cisneros, L. Santa-Taborda, L. Martínez Quintana, A.I.M. Rabee, H. Abed, N. Rockstroh, S. Bartling, M. Romero-Sáez, H. Atia, A. Belén Dongil, A. Brückner, J. Rabeah, The effect of O-

vacancies on intermediates stability and electron delocalization over MgO modified Ru/ZrO2: Spectroscopic insights during CO2 methanation, Chem. Eng. J., 474 (2023) 145646.
[48] S. Deng, Z. Qian, C. Zhu, B. Cheng, X. Wang, X. Fang, X. Xu, X. Wang, Boosting Low-Temperature CO2 Methanation Activity on Ru/Anatase-TiO2 Via Mn Doping: Revealing the Crucial Role of CO2 Dissociation, ACS Catal., 14 (2024) 16508-16521.
[49] S. Deng, C. Zhu, X. Fang, X. Xu, X. Wang, Lithium Cation Modification Markedly Enhances Ru Dispersion and CO2 Methanation Activity on Ru/SiO2 Catalysts, ACS Catal., 15 (2025) 7666-7676.
[50] S. Chen, A.M. Abdel-Mageed, M. Li, S. Cisneros, J. Bansmann, J. Rabeah, A. Brückner, A. Groß, R.J. Behm, Electronic metal-support interactions and their promotional effect on CO2 methanation on Ru/ZrO2 catalysts, J. Catal., 400 (2021) 407-420.
[51] S. Chen, A.M. Abdel-Mageed, M. Dyballa, M. Parlinska-Wojtan, J. Bansmann, S. Pollastri, L. Olivi, G. Aquilanti, R.J. Behm, Raising the COx Methanation Activity of a Ru/γ-Al2O3 Catalyst by Activated Modification of Metal–Support Interactions, Angew. Chem. Int. Ed., 59 (2020) 22763-22770.
[52] J. Feng, E. Hontañón, M. Blanes, J. Meyer, X. Guo, L. Santos, L. Paltrinieri, N. Ramlawi, L.C.P.M.d. Smet, H. Nirschl, F.E. Kruis, A. Schmidt-Ott, G. Biskos, Scalable and Environmentally Benign Process for Smart Textile Nanofinishing, ACS Applied Materials & Interfaces, 8 (2016) 14756-14765.
[53] J.H. Kwak, L. Kovarik, J. Szanyi, CO2 Reduction on Supported Ru/Al2O3 Catalysts: Cluster Size Dependence of Product Selectivity, ACS Catal., 3 (2013) 2449-2455.
[54] P. Panagiotopoulou, D.I. Kondarides, X.E. Verykios, Selective methanation of CO over supported Ru catalysts, Appl. Catal., B, 88 (2009) 470-478.
[55] X. Wang, Y. Hong, H. Shi, J. Szanyi, Kinetic modeling and transient DRIFTS–MS studies of CO2 methanation over Ru/Al2O3 catalysts, J. Catal., 343 (2016) 185-195.
[56] P. Panagiotopoulou, X.E. Verykios, Mechanistic Study of the Selective Methanation of CO over Ru/TiO2 Catalysts: Effect of Metal Crystallite Size on the Nature of Active Surface Species and Reaction Pathways, J. Phys. Chem. C, 121 (2017) 5058-5068.